npj | Computational Materials

www.nature.com/npjcompumats

ARTICLE OPEN

# Tunable ferromagnetic Weyl fermions from a hybrid nodal ring

Baobing Zheng[1,2,3], Bowen Xia[1], Rui Wang[1,4], Jinzhu Zhao[1], Zhongjia Chen[1,5], Yujun Zhao[5] and Hu Xu[1,6]

Realization of nontrivial band topology in condensed matter systems is of great interest in recent years. Using first-principles calculations and symmetry analysis, we propose an exotic topological phase with tunable ferromagnetic Weyl fermions in a half-metallic oxide $CrP_2O_7$. In the absence of spin–orbit coupling (SOC), we reveal that $CrP_2O_7$ possesses a hybrid nodal ring. When SOC is present, the spin-rotation symmetry is broken. As a result, the hybrid nodal ring shrinks to discrete nodal points and forms different types of Weyl points. The Fermi arcs projected on the (100) surface are clearly visible, which can contribute to the experimental study for the topological properties of $CrP_2O_7$. In addition, the calculated quasiparticle interference patterns are also highly desirable for the experimental study of $CrP_2O_7$. Our findings provide a good candidate of ferromagnetic Weyl semimetals, and are expected to realize related topological applications with their attracted features.

*npj Computational Materials* (2019)5:74 ; https://doi.org/10.1038/s41524-019-0214-z

## INTRODUCTION

Following the great advancements of topological insulators,[1,2] many efforts have been devoted to the studies of topological semimetals (TSMs) that also present topologically nontrivial band structures. TSMs mainly include Dirac,[3,4] Weyl,[5–10] and nodal line semimetals,[11–17] and so on, in which the valence and the conduction bands cross discretely or continuously in momentum space. The band crossings of TSMs can be topologically protected and thus are robust against the perturbations. Physically, the low-energy excitations near the crossing points can be regarded as the corresponding quasiparticles, namely Dirac, Weyl, and nodal line fermions, and so on.

Contrary to fourfold-degenerate Dirac fermions, Weyl fermions, a concept derived from the high energy particle physics and finally realized in Weyl semimetal (WSM) systems,[18] are twofold degenerate at the crossing points (i.e., Weyl points) with breaking either time-reversal or inversion symmetries. Owing to the Nielsen–Ninomiya "no-go theorem",[19,20] Weyl points severely appear in pairs with opposite chirality, and are merely annihilated with another Weyl point that has opposite chirality or by violating charge conservation.[21] There are two types of Weyl fermions in general. A type-I Weyl cone is only Lorentz invariant in the case of no tilting of the Weyl cone whatsoever. However, there is, in general, some tilting in condensed matter systems, just not enough to correspond to electron and hole pockets. In the case of a type-II Weyl cone, in contrast, tilting is severe enough that electron and hole pockets form.[10] WSMs that host unique Weyl fermions present nontrivial electronic structures, which leads to their topologically protected Fermi arc surface states, the negative magnetoresistance associated with the chiral anomaly, and anomalous Hall effect. These properties hold some potential applications for future electronic devices. Therefore, searching for WSMs with exotic topological properties is of great interest. The research of WSMs started from the magnetic pyrochlore iridates $Y_2Ir_2O_7$[5] and spinel $HgCr_2Se_4$,[6] in which the time-reversal symmetry $\mathcal{T}$ is broken. Subsequently, most of the reported WSMs are proposed in non-magnetic materials by breaking inversion symmetry $\mathcal{P}$.[7,10,22–24] Nevertheless, it is well known that the magnetism has the influence on the band topology and the topologically protected surface states. First, ferromagnetic WSMs can provide an intrinsic source of magnetic field to realize the enhanced anomalous Hall effect associated with the Weyl point near the Fermi level.[25] Second, the magnetic space group of crystal is sensitive to the magnetization directions, which leads to tunable Weyl points. Therefore, focusing on ferromagnetic WSMs is essential to study their exotic quantum phenomena related to magnetism. However, there are few candidates of magnetic WSMs,[26–28] even though they exerted an important influence on early work of WSMs.

In particular, the candidates of ferromagnetic WSMs that coexist in type-I and type-II Weyl points are highly desirable, because they exhibit rich topological physics. Recently, the concept of hybrid nodal ring that includes both type-I and type-II band-crossing points was proposed.[29,30] Zhang et al.[31] showed that the nonmagnetic material $Ca_2As$ hosts the hybrid nodal ring, and revealed that the hybrid nodal ring is characterized with unique signatures in magnetic response. In general, the nodal ring can be topologically protected by a combined $\mathcal{PT}$ symmetry or a mirror reflection symmetry. If these symmetries are broken, the hybrid nodal ring could shrink to several discrete crossing points, leading

[1]Department of Physics and Shenzhen Key Laboratory of Quantum Science and Engineering, Southern University of Science and Technology, 518055 Shenzhen, P. R. China; [2]School of Physics and Technology, Wuhan University, 430072 Wuhan, P. R. China; [3]College of Physics and Optoelectronic Technology and Advanced Titanium Alloys and Functional Coatings Cooperative Innovation Center, Baoji University of Arts and Sciences, 721016 Baoji, P. R. China; [4]Institute for Structure and Function and Department of physics, Chongqing University, 400044 Chongqing, P. R. China; [5]Department of Physics, South China University of Technology, 510640 Guangzhou, P. R. China and [6]Center for Quantum Computing, Peng Cheng Laboratory, 518055 Shenzhen, P. R. China
Correspondence: Hu Xu (xuh@sustech.edu.cn)
These authors contributed equally: Baobing Zheng, Bowen Xia, Rui Wang

Received: 20 March 2019 Accepted: 26 June 2019
Published online: 15 July 2019

to the emergence of type-I and type-II Weyl points.[32] Therefore, one of the possible routes to realizing ferromagnetic WSMs coexisting in type-I and type-II Weyl points is to introduce spin–orbit coupling (SOC) for the hybrid nodal ring in ferromagnetic materials. In this work, we propose that the ferromagnetic $CrP_2O_7$ possesses a hybrid nodal ring when SOC is absent. After introducing SOC, we found that $CrP_2O_7$ is ferromagnetic WSM coexisting type-I and type-II Weyl points. Moreover, the band topology of $CrP_2O_7$ can be manipulated with magnetization directions. To facilitate the experimental investigation, we also calculated the surface states and the joint density of states (JDOSs) associated with quasiparticle interference (QPI) pattern of $CrP_2O_7$.

## RESULTS AND DISCUSSION

The crystal structure of monoclinic $CrP_2O_7$ is illustrated in Fig. 1a, which belongs to the non-symmorphic space group of $P2_1/c$ ($C_{2h}$) with four formula units in the primitive cell. Its optimized lattice parameters and atomic Wyckoff positions are summarized in Supplementary Table 1. Clearly, the structure consists of the distorted $PO_4$ tetrahedrons, with P being their center and $CrO_6$ octahedrons with Cr occupying their center. The phonon spectrum (see Supplementary Fig. 1) indicates that the monoclinic $CrP_2O_7$ is dynamically stable. In addition, to assess its thermodynamic stability, we also calculated the formation enthalpy of $CrP_2O_7$. The chemical composition of $CrP_2O_7$ can be decomposed to chromium dioxide ($CrO_2$) and diphosphorus pentaoxide ($P_2O_5$), and therefore we chose rutile $CrO_2$[33] and orthorhombic $P_2O_5$[34] as the reference phases. As a result, the formation energy of $CrP_2O_7$ can be defined by $\Delta E_f = E(CrP_2O_7) - E(CrO_2) - E(P_2O_5)$, in which $E(CrP_2O_7)$, $E(CrO_2)$, and $E(P_2O_5)$ are the total energies of $CrP_2O_7$, rutile $CrO_2$, and orthorhombic $P_2O_5$, respectively. The negative formation energy of −1.396 eV per unit cell indicates that the $CrP_2O_7$ is thermodynamically stable and is feasible to be experimentally synthesized.

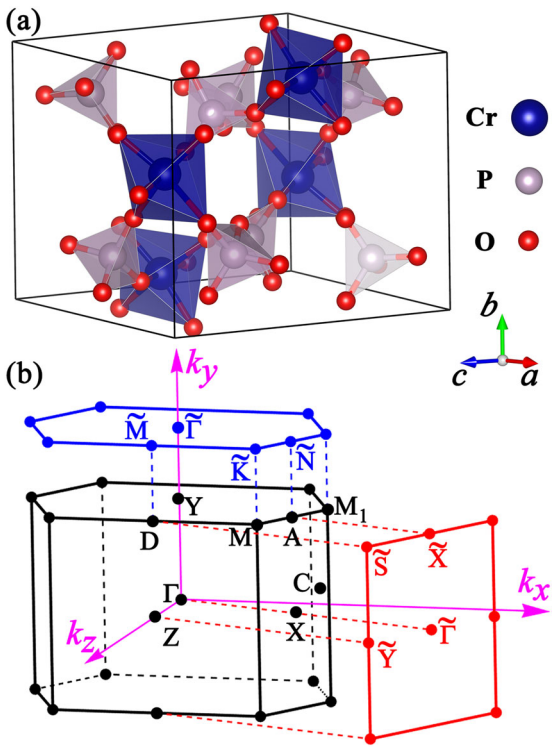


**Fig. 1** Crystal structure and Brillouin zone (BZ). **a** Crystal structure of monoclinic $CrP_2O_7$ with space group of $P2_1/c$. Cr, P, and O atoms are represented by blue, purple, and red spheres, respectively. **b** The bulk BZ, and the projected surface BZ of (100) and (010) planes for $CrP_2O_7$. The high-symmetry points are marked by black, red, and blue dots for bulk BZ, (100) surface BZ, and (010) surface BZ, respectively

To determine the magnetic configuration of $CrP_2O_7$, we performed total energy calculations on various magnetic phases for the monoclinic $CrP_2O_7$. Our calculations show that the ferromagnetic phases are the most energetically favorable (at least 45.2 meV per Cr atom lower in energy than the collinear and noncollinear antiferromagnetic phases, see details in Supplementary Table 2). The calculated magnetic moment per Cr atom is $2\mu_B$. Moreover, the ferromagnetic phases with different magnetization directions are almost degenerate, suggesting that the magnetization directions of soft magnetic $CrP_2O_7$ can be easily manipulated by external magnetic field.

To study the band topology, we first calculated the band structure of $CrP_2O_7$ without SOC, as shown in Fig. 2a. Clearly, $CrP_2O_7$ presents the half-metallic behavior. The majority-spin channel is metallic, while there is a gap of 4.03 eV for the minority-spin channel. Along the *Y*–Γ direction in momentum space, there exists one type-II band crossing with the electron- and hole-like states coexisting in energy. Along the other high symmetry lines, we do not find any band-crossing points associated with the valence and conduction bands.

To further find all band crossings in the whole Brillouin zone (BZ), we constructed the tight-binding Hamiltonian by fitting the band structures. Then, all the nodes are obtained based on the tight-binding Hamiltonian. As a result, we found that the nodes in the BZ form a closed nodal ring, which is centered around the Γ point, as shown in Fig. 2b, c. Owing to the existence of glide mirror for $CrP_2O_7$, the nodal ring satisfies the mirror reflection with respect to the (010) plane. From the projection of nodal ring onto the (010) plane, we can clearly see that the nodal ring goes across the first BZ and partly locates in the second BZ (see Fig. 2c). The calculated Berry phases $\gamma$ along a closed loop $\mathcal{L}$ that encircles the nodal ring, defined by $\gamma = \oint_{\mathcal{L}} \mathcal{A}(\mathbf{k}) \cdot d\mathbf{k}$ [$\mathcal{A}(\mathbf{k})$ is Berry connection], are plotted in Fig. 2d along the high-symmetry lines *Y*–Γ–*Y*. The obtained results confirm the nontrivial topology of the nodal ring in ferromagnetic $CrP_2O_7$. In addition to the type-II band crossings, we also found that the nodal ring contains type-I band crossings. For example, the band structure around the crossing point (0.350, 0.0, −0.518) shows that the two bands cross linearly with electron- and hole-like states occupying different energy ranges (see Fig. 2e), characteristic of the type-I band crossings. The coexistence of type-I and type-II band crossings suggests that the hybrid nodal ring exists in the ferromagnetic $CrP_2O_7$.

Next, we show the nodal ring solution based on the two-band $k \cdot p$ effective Hamiltonian, which can be described as

$$H(\mathbf{k}) = \sum_{i=0}^{3} d_i(\mathbf{k})\sigma_i, \tag{1}$$

where $\sigma_0$ is $2 \times 2$ identity matrix and $\sigma_1$, $\sigma_2$, $\sigma_3$ represent the Pauli matrices, respectively, $d_i(\mathbf{k})$ are real functions, in which $\mathbf{k} = (k_x, k_y, k_z)$ are three components of the momentum $\mathbf{k}$ with respect to the Γ point. Because the kinetic term $d_0(\mathbf{k})\sigma_0$ is independent with the band crossings, we ignore it in the following discussions. Consider the inversion symmetry of the crystal structure, we can choose it as $\mathcal{P} = \sigma_z$. Under this symmetry, we can obtain

$$H(\mathcal{P}\mathbf{k}) = \mathcal{P}H(\mathbf{k})\mathcal{P}^{-1}, \tag{2}$$

which translates into

$$d_{1,2}(\mathbf{k}) = -d_{1,2}(-\mathbf{k}), \quad d_3(\mathbf{k}) = d_3(-\mathbf{k}). \tag{3}$$

When SOC is absent, the majority spin and the minority spin can be clearly distinguished because they cannot hybridize with each other. Because this nodal ring locates near the Fermi level, there exists only the states of one spin. The spin flip can only occur by acting on the time-reversal operation $\mathcal{T}$, which assures that the

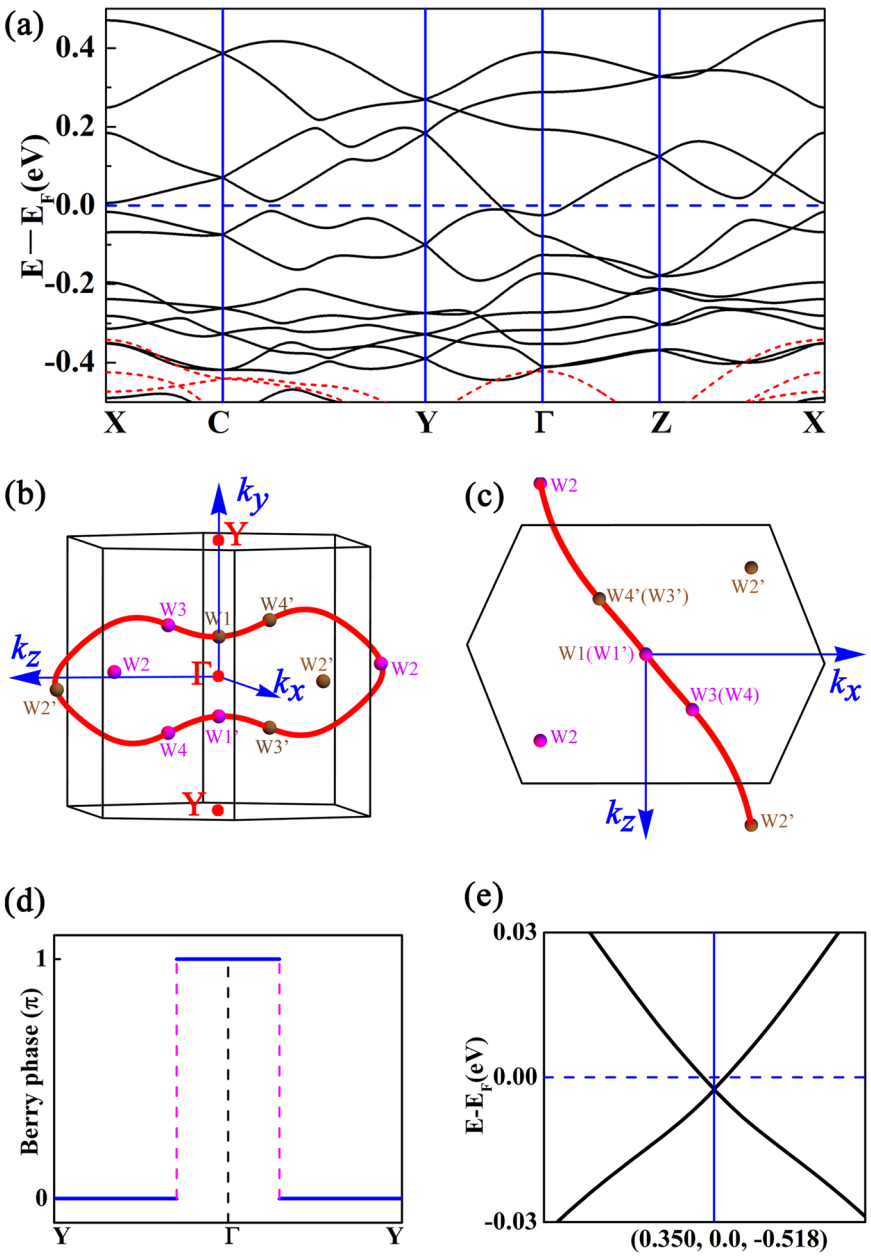


**Fig. 2** Band structure, hybrid nodal ring, and the variation of Berry phase. **a** Band structure of monoclinic $CrP_2O_7$ without spin–orbit coupling (SOC). The black solid lines and the red dotted lines represent the majority- and minority-spin bands, respectively. The hybrid nodal ring (**b**) and its projection (**c**) onto the (010) plane in the Brillouin zone (BZ), in which the magenta and brown spheres denote the Weyl points (one pair along the [0 1 0] and three pairs along the [1 0 0] magnetization directions with SOC) with chirality +1 and −1, respectively. The Weyl point of W2 is type-I, while W1, W3, and W4 are type-II. The equivalent Weyl points of W2 and W2′ in the first BZ are also labeled. **d** The variation of Berry phase along the high-symmetry *Y*–Γ–*Y* paths in the $k_x = 0$ plane. **d** The band structure around the type-I band crossing (0.350, 0.0, −0.518) point. In **a**, **e**, the blue dashed lines denote the Fermi level ($E_F$)

two-band $k \cdot p$ effective Hamiltonian is invariant under $\mathcal{T}$ symmetry, namely,

$$H(\mathcal{T}\mathbf{k}) = \mathcal{T}H(\mathbf{k})\mathcal{T}^{-1}. \tag{4}$$

In the absence of SOC, the time-reversal operation can be chosen as $\mathcal{T} = K$ in terms of $\mathcal{T}^2 = +1$, where $K$ is the complex conjugation. Thus, Eq. (4) can be simplified into

$$d_{1,3}(\mathbf{k}) = d_{1,3}(-\mathbf{k}), \quad d_2(\mathbf{k}) = -d_2(-\mathbf{k}). \tag{5}$$

From Eqs. (3) and (5), we can obtain the following expressions constrained by the inversion and time-reversal symmetries:

$$\begin{aligned} d_1(\mathbf{k}) &= 0, \\ d_2(\mathbf{k}) &= \sum_{i=x,y,z} A_i k_i + \sum_{i,j,l=x,y,z} A_{ijl} k_i k_j k_l, \\ d_3(\mathbf{k}) &= B + \sum_{i,j=x,y,z} B_{ij} k_i k_j + \sum_{i,j,l,m=x,y,z} B_{ijlm} k_i k_j k_l k_m, \end{aligned} \tag{6}$$

where the parameters $A_i$, $A_{ijl}$, $B$, $B_{ij}$, and $B_{ijlm}$ derived from the $k \cdot p$ model can be determined by the first-principles calculations. For simplicity, we can ignore the high-order terms of $d_2(\mathbf{k})$ and $d_3(\mathbf{k})$ in Eq. (6). Meanwhile, considering that the little group is $C_s$ in the

$k_x$–$k_z$ plane, we can simplify $d_2(\mathbf{k})$ and $d_3(\mathbf{k})$ of Eq. (6) into

$$d_2(\mathbf{k}) = A_x k_x + A_y k_y + A_z k_z,$$
$$d_3(\mathbf{k}) = B + B_{xx}k_x^2 + B_{yy}k_y^2 + B_{zz}k_z^2 + B_{xz}k_x k_z. \quad (7)$$

Based on above discussions, we can determine the energy dispersion as

$$E(\mathbf{k}) = \pm\sqrt{d_2(\mathbf{k})^2 + d_3(\mathbf{k})^2}. \quad (8)$$

Thus, the valence and conduction bands can touch only when the conditions of $d_2(\mathbf{k}) = 0$ and $d_3(\mathbf{k}) = 0$ are satisfied simultaneously, which allow the codimension of the band crossing that is one, resulting in the formation of a nodal ring in momentum space. From Eq. (7), we can see that $d_2(\mathbf{k}) = 0$ is the equation of a plane across the Γ point. In addition, if the conditions of $B_{xx} > 0$, $B_{yy} > 0$, $B_{zz} > 0$, and $B < 0$ are satisfied, $d_3(\mathbf{k}) = 0$ can represent the equation of a closed ellipsoidal surface centered at the Γ point. Certainly, $B_{xx} < 0$, $B_{yy} < 0$, $B_{zz} < 0$, and $B > 0$ can also result in the solution of a closed ellipsoidal surface centered at the Γ point for $d_3(\mathbf{k}) = 0$. As a consequence, the intersection of the plane $d_2(\mathbf{k}) = 0$ and the closed ellipsoidal surface $d_3(\mathbf{k}) = 0$ forms the closed nodal ring. Due to existence of only $k_x k_z$ cross-term, the nodal ring must cross the $k_y$ axis and is located in the quadrants 1 and 3 of $k_x$–$k_z$ plane, as shown in Fig. 2b, c. Note that the detailed shape of the closed nodal ring is determined by the high-order terms in Eq. (6).

When SOC is included, the two spin channels couple together and the spin-rotation symmetry that protects the nodal ring is broken. Thus, the hybrid nodal ring shall shrink to discrete points and form different types of Weyl points. We firstly provide a parity analysis for the band topology because of the presence of $\mathcal{P}$ symmetry for $CrP_2O_7$. The calculated parity products of occupied Bloch states at the time-reversal invariant momenta (TRIM) points are +1 except the Γ points, which leads to the fact that the product of parity eigenvalues at eight TRIM points is −1, suggesting that there exists odd number of pairs of Weyl points in the bulk.[35] Consider that the magnetic symmetry is closely related to the magnetization direction and hence has a significant impact on the topological properties of ferromagnetic materials. Here, we mainly focus on two typical magnetic directions, that is, [0 1 0] and [1 0 0] magnetization directions. As listed in Table 1, there exist one pair of Weyl fermions along the [0 1 0] magnetization direction and three pairs of Weyl fermions along the [1 0 0]

**Table 1.** The Weyl points ($k_x$, $k_y$, $k_z$) in Cartesian coordinates along [0 1 0] and [1 0 0] magnetization **M** directions, the corresponding Chern numbers ($\mathcal{C}$), energies with respect to the Fermi level, and types of Weyl points are listed

| M | Nodal point | Position (Å$^{-1}$) | $E - E_F$ (meV) | $\mathcal{C}$ | Type |
|---|---|---|---|---|---|
| [0 1 0] | W1 | (0.0, 0.1126, 0.0) | −14 | −1 | II |
| [1 0 0] | W2 | (−0.3108, 0.020, 0.2581) | −1 | +1 | I |
| | W3 | (0.1374, 0.1521, 0.1634) | 6 | +1 | II |
| | W4 | (0.1374, −0.1521, 0.1634) | 6 | +1 | II |

The coordinates of the other Weyl point with opposite chiralities are related to the $\mathcal{P}$ symmetry

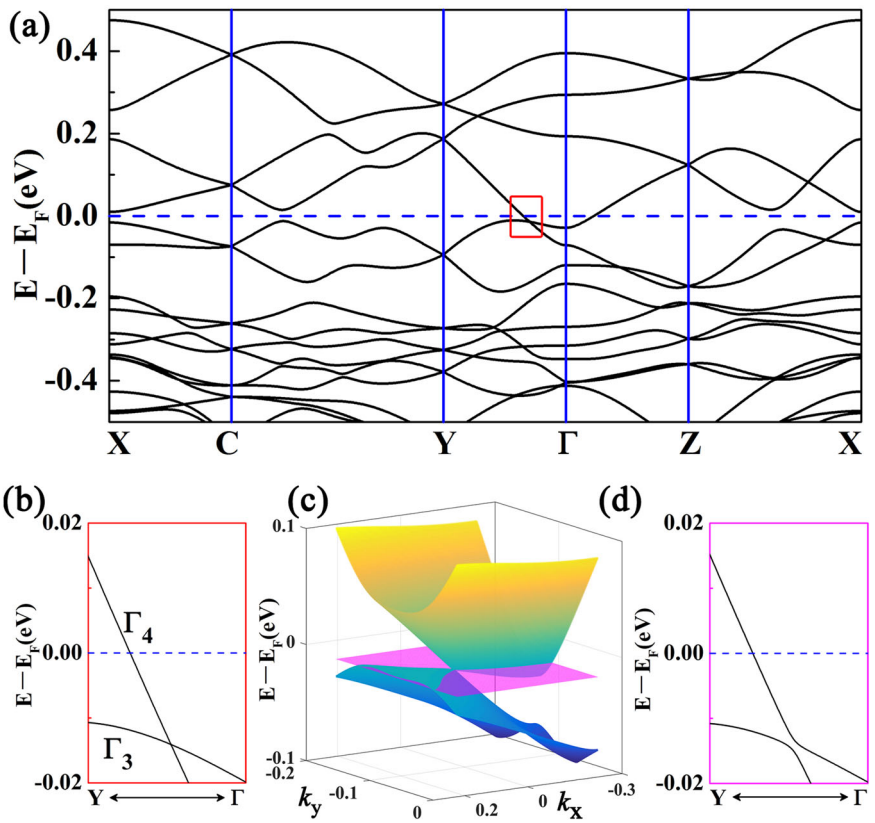


**Fig. 3** Band structure. **a** Band structure of $CrP_2O_7$ in the presence of spin–orbit coupling (SOC). **b** The enlarged two crossing $\Gamma_3$ and $\Gamma_4$ bands along *Y*–Γ direction within the [0 1 0] magnetization direction. **c** The three-dimensional (3D) representation of band structure around the Weyl point W1 within the [0 1 0] magnetization direction, and the electron and hole pockets occur at this point. The light purple plane denotes the reference constant energy plane corresponding to the W1 Weyl point. **d** The enlarged valence and conduction bands along *Y*–Γ direction within the [1 0 0] magnetization direction. The Fermi level ($E_F$) is marked with the blue dashed line

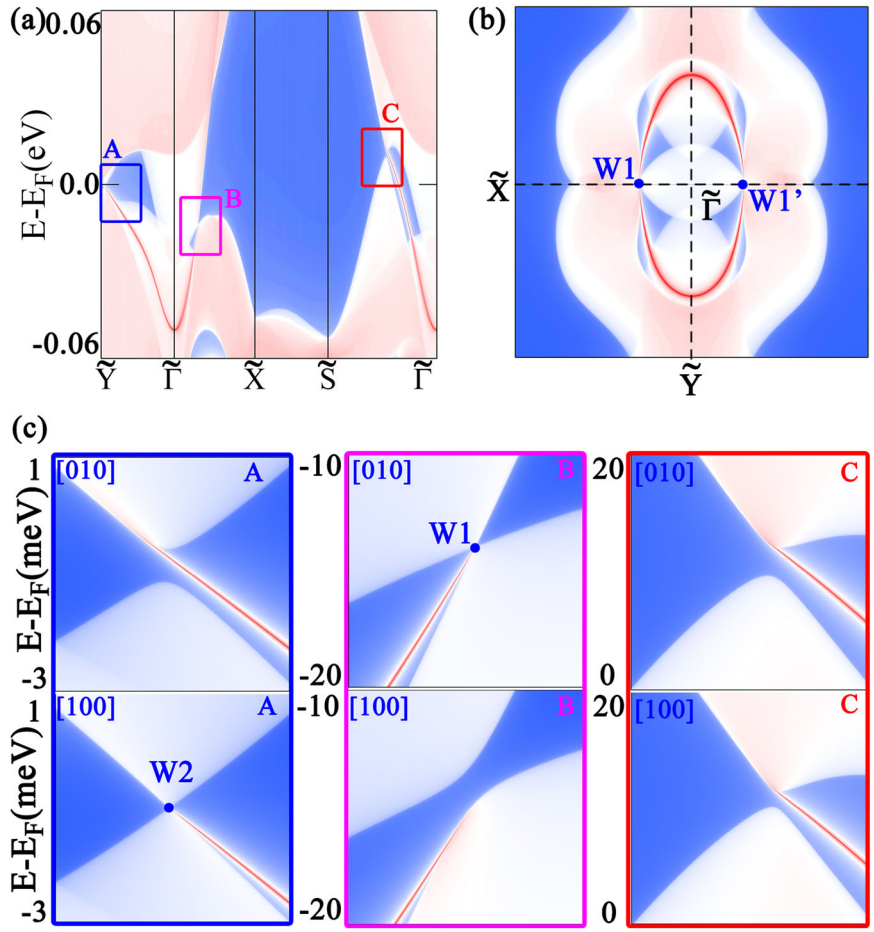


**Fig. 4** Topological surface states. **a** The surface states of projected (100) plane for $CrP_2O_7$. **b** Fermi arcs at the energy of $E - E_F = -14$ meV of $CrP_2O_7$ within the [0 1 0] magnetization direction, and the Weyl points are marked with blue dots. **c** The A, B and C regions denoted by blue, magenta, and red rectangles are enlarged from left to right with different magnetization directions, the top panels are the surface states along [0 1 0] magnetization direction, while the bottom panels denote the [1 0 0] magnetization direction, respectively

magnetization direction, respectively, which is consistent with our parity analysis.

With the magnetization along the [0 1 0] direction, the magnetic double point group $C_{2h}$ is preserved. Along the $Y$–Γ direction in momentum space, the little group is $C_2$, which can allow for the band crossing along this direction, thus resulting in type-II Weyl point W1 (0.0, 0.1126, 0.0) below the Fermi level, as listed in Table 1. The two crossing bands belong to different irreducible representations of $C_2$ operation, namely $\Gamma_3$ and $\Gamma_4$, as shown in Fig. 3a, b. Certainly, another type-II Weyl point must appear at W1′ (0.0, −0.1126, 0.0) with opposite Chern number in view of the $\mathcal{P}$ symmetry. It is well known that the type-II Weyl point appears as the contact point between electron and hole pockets, characteristic of the open constant energy surfaces. The 3D representation of band structure is shown in Fig. 3c, implying that the Weyl fermion with breaking Lorentz invariance (i.e., type-II Weyl fermion) appears. In addition, we can observe the electron and hole pockets from the Fermi surface at the (001) plane (see Supplementary Fig. 2), which further confirm that these points are type-II.

Along the [1 0 0] magnetization direction, the magnetic double point group is reduced to $C_i$. Consequently, the screw-rotation symmetry is broken, which leads to the fact that the Weyl points along $Y$–Γ without SOC open a tiny gap when the magnetization is along the [1 0 0] direction, as shown in Fig. 3d. However, we find other three pairs of Weyl points that do not locate along the high symmetry lines or planes (see Table 1), implying that these band crossings are accidental. The three pairs of Weyl points contain one pair of type-I (W2) and two pairs of type-II (W3 and W4) Weyl points. The band structures and their 3D representations around the type-I W2 and type-II W3 Weyl points are shown in Supplementary Fig. 3. The corresponding Chern numbers are calculated by using Wilson-loop method as implemented in Z2Pack package,[36] which are also summarized in Table 1. To check the topological stability of the coexistence of the type-I and type-II Weyl points, we tuned the the strength of SOC with $0.8\lambda_0$ and $1.2\lambda_0$ (here $\lambda_0$ denotes the actual SOC strength). The calculated results suggest that the SOC strength can only slightly change the positions of Weyl nodes. Along the [0 1 0] and [1 0 0] magnetization directions, the type-I and type-II Weyl points remain present, dictating that the topological properties of $CrP_2O_7$ are robust against perturbation.

The evident manifestation of WSMs is the existence of the topologically protected surface states and the visible Fermi arcs. As shown in Fig. 4, the obtained surface states of $CrP_2O_7$ within the [0 1 0] magnetization direction show clear connection between the valence and conduction bands on the (100) surface. The type-II Weyl point W1 located along the $Y$–Γ direction is projected onto the $\tilde{X}$–$\tilde{\Gamma}$ direction of the (100) surface, and the tilted cone is therefore observed (see Fig. 4c). Along $\tilde{Y}$–$\tilde{\Gamma}$ and $\tilde{S}$–$\tilde{\Gamma}$ directions, the small topologically nontrivial gaps are observed. When magnetization is along the [1 0 0] direction, the $C_2$ symmetry is broken. Thus, the surface states on the (100) plane show a nontrivial gap along the projected $\tilde{X}$–$\tilde{\Gamma}$ direction. However,

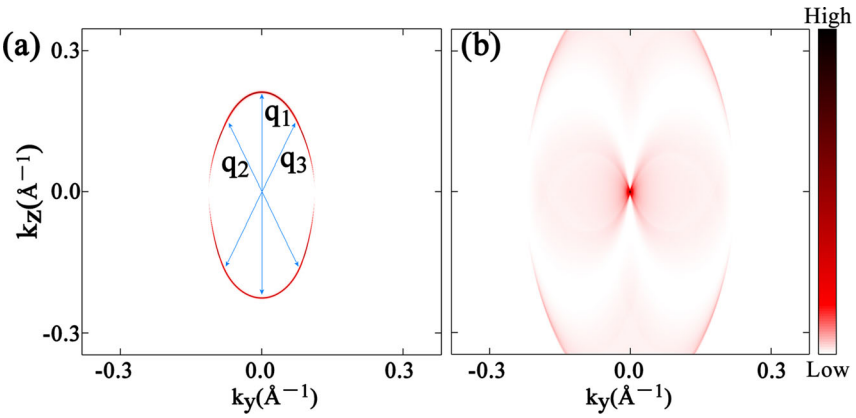


**Fig. 5** Fermi arcs and quasiparticle interference (QPI) patterns. The weighted Fermi arcs (**a**) and joint density of states (JDOS) (**b**) of $CrP_2O_7$ on the (100) surface. The energetically allowed scattering vectors in first Brillouin zone (BZ) associated with the QPI patterns are denoted by $q_1$, $q_2$, and $q_3$

we can clearly see a type-I cone along $\tilde{Y}$–$\tilde{\Gamma}$ direction. This cone originates from the type-I Weyl point W2, which can be projected on $\tilde{Y}$–$\tilde{\Gamma}$ direction of the (100) plane. The accidentally degenerate W3 and W4, forming tilted cons, can also be found in the surface states on the (100) plane if the suitable $k$ paths are selected in the projected BZ. In addition, the nontrivial Fermi arc states are visible in the projected (100) surface (see Fig. 4b), which contributes to be experimentally observed in angle-resolved photoemission spectroscopy (ARPES). However, we cannot find the Fermi arc on the projected (010) surface, which is ascribed to the fact that the two Weyl points along the $Y$–Γ direction are projected to one point on the (010) surface. Along the [1 0 0] magnetization direction, the visible Fermi arc states projected on the (010) plane are also observed (see Supplementary Fig. 4).

QPI pattern can directly signify the momentum transformation across the Fermi arc surface state, which provides deep insight into the surface states of WSMs in momentum space based on spectroscopic-imaging scanning tunneling microscopy, and is considered to be good complementarity to ARPES.[37] The QPI pattern corresponds to the Fourier transform of a real-space local density of states map and can be approximately interpreted in terms of JDOSs:[38,39]

$$J(\mathbf{q},\omega) = \int d^2\mathbf{k}\rho^0(\mathbf{k},\omega)\rho^0(\mathbf{k}-\mathbf{q},\omega), \tag{9}$$

and $\rho^0(\mathbf{k},\omega) = -\frac{1}{\pi}\mathbf{Im}G^0(\mathbf{k},\omega)$ is **k**-resolved surface density of states, where $G^0(\boldsymbol{k},\omega)$ denotes surface Green function at surface momentum **k** and a given energy $\omega$, and **q** is the scattering vector. As plotted in Fig. 5, the calculated weighted Fermi arcs show an approximately constant spectral density. From the Fermi arcs, we can identify three independent scattering vectors (labeled as $q_1$, $q_2$, and $q_3$) arising from arc–arc scattering. Figure 5b shows visible QPI pattern of $CrP_2O_7$. The highest intensity patterns appear at the Γ point, which can be ascribed to the fact that $q_1$, $q_2$, and $q_3$ scatterings are all contributed to the QPI pattern of the Γ point.

In summary, multiple nontrivial fermions are explored in the ferromagnetic $CrP_2O_7$ employing the first-principles calculations and symmetry analysis. This ferromagnetic material possesses the hybrid nodal ring with coexistence of type-I and type-II band crossings. The nodal ring is demonstrated by employing a two-band $k\cdot p$ effective Hamiltonian. Moreover, the hybrid nodal ring becomes the discrete type-I and type-II Weyl fermions when SOC is considered. The interplay between the magnetization directions and crystal symmetries in $CrP_2O_7$ is discussed in detail using symmetry analysis. The calculated Fermi arc surface states and QPI patterns are highly desirable for the experimental study. We expect that our results can be helpful in understanding the ferromagnetic WSMs and realizing the topological properties of $CrP_2O_7$ in experiments.

## METHODS

We performed first-principles calculations within the framework of density functional theory[40,41] as implemented in the Vienna Ab initio Simulation Package.[42] The generalized gradient approximation (GGA) combined with the Perdew–Burke–Ernzerhof functional[43] was chosen to describe the exchange correlation interactions. The electron and core interactions were described by the projector augmented-wave method,[44] in which the $3p^6 3d^5 4s^1$, $3s^2 3p^3$ and $2s^2 2p^4$ were treated as the valence electrons for Cr, P, and O, respectively. The kinetic-energy cutoff for plane-wave basis set used was 600 eV. Considering the strong correlation effect of 3*d* electron of Cr, we employed the GGA + $U$ scheme[45] with an effective on-site Coulomb energy $U_{\mathrm{eff}} = U - J = 3.6$ eV. It is worth noting that the topological properties of $CrP_2O_7$ can be obtained in a $U_{\mathrm{eff}}$ range from 2.6 to 4 eV, which works well on other compounds including Cr atoms.[46–48] The influence of the exchange coupling $J$ on the band structure of $CrP_2O_7$ is also discussed in Supplementary Fig. 5. The tight-binding Hamiltonian was constructed by the maximally localized Wannier functions basis as implemented in Wannier90 code.[49] Based on the tight-binding Hamiltonian, the iterative Green function method as implemented in WannierTools package[50] was employed to calculate the surface states, Fermi arcs, and the joint density of states.

## DATA AVAILABILITY

The data that support the findings of this study are available from the corresponding author on reasonable request.

## ACKNOWLEDGEMENTS

This work is supported by the National Natural Science Foundation of China (NSFC, Grant Nos. 11674148, 11334003, and 11847301), the Guangdong Natural Science Funds for Distinguished Young Scholars (No. 2017B030306008), the Fundamental Research Funds for the Central Universities (Nos. cqu2018CDHB1B01, 2019CDXYWL0029, and 2019CDJDWL0005), the China Postdoctoral Science Foundation (No. 2019M652686), the Natural Science Basic Research plan in Shaanxi Province of China (Grant No. 2018JQ1083), the Scientific Research Program Funded by Shaanxi Provincial Education Department (Grant No. 17JK0041), the Baoji University of Arts and Sciences Key Research (Grant No.: ZK2017009), and the Science, Technology, and Innovation Commission of Shenzhen Municipality (No. ZDSYS20170303165926217).

## AUTHOR CONTRIBUTIONS

H.X. directed and designed the whole research. B.B.Z. did all calculations and wrote the paper. B.W.X. initiated the research and did early calculations. R.W. provided scientific discussions. All authors discussed the results and provided inputs to the manuscript.

## ADDITIONAL INFORMATION

**Supplementary Information** accompanies the paper on the *npj Computational Materials* website (https://doi.org/10.1038/s41524-019-0214-z).

**Competing interests:** The authors declare no competing interests.

**Publisher's note:** Springer Nature remains neutral with regard to jurisdictional claims in published maps and institutional affiliations.

## REFERENCES

1. Hasan, M. Z. & Kane, C. L. Colloquium: topological insulators. *Rev. Mod. Phys.* **82**, 3045–3067 (2010).
2. Qi, X.-L. & Zhang, S.-C. Topological insulators and superconductors. *Rev. Mod. Phys.* **83**, 1057–1110 (2011).
3. Liu, Z. K. et al. Discovery of a three-dimensional topological Dirac semimetal, $Na_3Bi$. *Science* **343**, 864–867 (2014).
4. Young, S. M. et al. Dirac semimetal in three dimensions. *Phys. Rev. Lett.* **108**, 140405 (2012).
5. Wan, X., Turner, A. M., Vishwanath, A. & Savrasov, S. Y. Topological semimetal and Fermi-arc surface states in the electronic structure of pyrochlore iridates. *Phys. Rev. B* **83**, 205101 (2011).
6. Xu, G., Weng, H., Wang, Z., Dai, X. & Fang, Z. Chern semimetal and the quantized anomalous Hall effect in $HgCr_2Se_4$. *Phys. Rev. Lett.* **107**, 186806 (2011).
7. Weng, H., Fang, C., Fang, Z., Bernevig, B. A. & Dai, X. Weyl semimetal phase in noncentrosymmetric transition-metal monophosphides. *Phys. Rev. X* **5**, 011029 (2015).
8. Lv, B. Q. et al. Experimental discovery of Weyl semimetal TaAs. *Phys. Rev. X* **5**, 031013 (2015).
9. Yu, Z.-M., Yao, Y. & Yang, S. A. Predicted unusual magnetoresponse in type-II Weyl semimetals. *Phys. Rev. Lett.* **117**, 077202 (2016).
10. Soluyanov, A. A. et al. Type-II Weyl semimetals. *Nature* **527**, 495 (2015).
11. Burkov, A. A., Hook, M. D. & Balents, L. Topological nodal semimetals. *Phys. Rev. B* **84**, 235126 (2011).
12. Wang, R. et al. Nodal line fermions in magnetic oxides. *Phys. Rev. B* **97**, 241111 (2018).
13. Yu, R., Weng, H., Fang, Z., Dai, X. & Hu, X. Topological node-line semimetal and Dirac semimetal state in antiperovskite $Cu_3PdN$. *Phys. Rev. Lett.* **115**, 036807 (2015).
14. Li, S. et al. Nonsymmorphic-symmetry-protected hourglass Dirac loop, nodal line, and Dirac point in bulk and monolayer $X_3SiTe_6$ ($X$ = Ta, Nb). *Phys. Rev. B* **97**, 045131 (2018).
15. Yang, S. A., Pan, H. & Zhang, F. Dirac and Weyl superconductors in three dimensions. *Phys. Rev. Lett.* **113**, 046401 (2014).
16. Weng, H. et al. Topological node-line semimetal in three-dimensional graphene networks. *Phys. Rev. B* **92**, 045108 (2015).
17. Chen, Y. et al. Nanostructured carbon allotropes with Weyl-like loops and points. *Nano Lett.* **15**, 6974–6978 (2015).
18. Weyl, H. Elektron und gravitation. *I. Z. Phys.* **56**, 330–352 (1929).
19. Nielsen, H. & Ninomiya, M. Absence of neutrinos on a lattice: (I). Proof by homotopy theory. *Nucl. Phys. B* **185**, 20–40 (1981).
20. Nielsen, H. & Ninomiya, M. Absence of neutrinos on a lattice: (II). Intuitive topological proof. *Nucl. Phys. B* **193**, 173–194 (1981).
21. Hosur, P. & Qi, X. Recent developments in transport phenomena in Weyl semimetals. *C. R. Phys.* **14**, 857–870 (2013).
22. Xu, S.-Y. et al. Discovery of a Weyl fermion semimetal and topological Fermi arcs. *Science* **349**, 613–617 (2015).
23. Lu, L. et al. Experimental observation of Weyl points. *Science* **349**, 622–624 (2015).
24. Shekhar, C. et al. Extremely large magnetoresistance and ultrahigh mobility in the topological Weyl semimetal candidate NbP. *Nat. Phys.* **11**, 645 (2015).
25. Burkov, A. A. Anomalous Hall effect in Weyl metals. *Phys. Rev. Lett.* **113**, 187202 (2014).
26. Yang, H. et al. Topological Weyl semimetals in the chiral antiferromagnetic materials $Mn_3Ge$ and $Mn_3Sn$. *New J. Phys.* **19**, 015008 (2017).
27. Wang, R. et al. Ferromagnetic Weyl fermions in $CrO_2$. *Phys. Rev. B* **97**, 195157 (2018).
28. Wang, Q. et al. Large intrinsic anomalous Hall effect in half-metallic ferromagnet $Co_3Sn_2S_2$ with magnetic Weyl fermions. *Nat. Commun.* **9**, 3681 (2018).
29. Li, S. et al. Type-II nodal loops: theory and material realization. *Phys. Rev. B* **96**, 081106 (2017).
30. Chen, C. et al. Weyl-loop half-metal in $Li_3(FeO_3)_2$. *Phys. Rev. B* **99**, 075131 (2019).
31. Zhang, X. et al. Hybrid nodal loop metal: unconventional magnetoresponse and material realization. *Phys. Rev. B* **97**, 125143 (2018).
32. Yu, R., Wu, Q., Fang, Z. & Weng, H. From nodal chain semimetal to Weyl semimetal in HfC. *Phys. Rev. Lett.* **119**, 036401 (2017).
33. Cloud, W. H., Schreiber, D. S. & Babcock, K. R. X-ray and magnetic studies of $CrO_2$ single crystals. *J. Appl. Phys.* **33**, 1193–1194 (1962).
34. Stachel, D., Svoboda, I. & Fuess, H. Phosphorus pentoxide at 233 K. *Acta Crystallogr. C.* **51**, 1049–1050 (1995).
35. Wang, Z. et al. Time-reversal-breaking Weyl fermions in magnetic Heusler alloys. *Phys. Rev. Lett.* **117**, 236401 (2016).
36. Gresch, D. et al. Z2pack: numerical implementation of hybrid Wannier centers for identifying topological materials. *Phys. Rev. B* **95**, 075146 (2017).
37. Zheng, H. & Hasan, M. Z. Quasiparticle interference on type-I and type-II Weyl semimetal surfaces: a review. *Adv. Phys. X* **3**, 1466661 (2018).
38. Derry, P. G., Mitchell, A. K. & Logan, D. E. Quasiparticle interference from magnetic impurities. *Phys. Rev. B* **92**, 035126 (2015).
39. Kourtis, S., Li, J., Wang, Z., Yazdani, A. & Bernevig, B. A. Universal signatures of Fermi arcs in quasiparticle interference on the surface of Weyl semimetals. *Phys. Rev. B* **93**, 041109 (2016).
40. Kohn, W. & Sham, L. J. Self-consistent equations including exchange and correlation effects. *Phys. Rev.* **140**, A1133–A1138 (1965).
41. Hohenberg, P. & Kohn, W. Inhomogeneous electron gas. *Phys. Rev.* **136**, B864–B871 (1964).
42. Kresse, G. & Furthmüller, J. Efficient iterative schemes for ab initio total-energy calculations using a plane-wave basis set. *Phys. Rev. B* **54**, 11169–11186 (1996).
43. Perdew, J. P., Burke, K. & Ernzerhof, M. Generalized gradient approximation made simple. *Phys. Rev. Lett.* **77**, 3865–3868 (1996).
44. Kresse, G. & Joubert, D. From ultrasoft pseudopotentials to the projector augmented-wave method. *Phys. Rev. B* **59**, 1758–1775 (1999).
45. Dudarev, S. L., Botton, G. A., Savrasov, S. Y., Humphreys, C. J. & Sutton, A. P. Electron-energy-loss spectra and the structural stability of nickel oxide: an LSDA + U study. *Phys. Rev. B* **57**, 1505–1509 (1998).
46. Korotin, M. A., Anisimov, V. I., Khomskii, D. I. & Sawatzky, G. A. $CrO_2$: a self-doped double exchange ferromagnet. *Phys. Rev. Lett.* **80**, 4305–4308 (1998).
47. Weng, H., Kawazoe, Y., Wan, X. & Dong, J. Electronic structure and optical properties of layered perovskites $Sr_2MO_4$ ($M$ = Ti, V, Cr, and Mn): an ab initio study. *Phys. Rev. B* **74**, 205112 (2006).
48. Ederer, C. & Komelj, M. Magnetic coupling in $CoCr_2O_4$ and $MnCr_2O_4$: an LSDA + U study. *Phys. Rev. B* **76**, 064409 (2007).
49. Mostofi, A. A. et al. Wannier90: a tool for obtaining maximally-localised Wannier functions. *Comput. Phys. Commun.* **178**, 685–699 (2008).
50. Wu, Q., Zhang, S., Song, H.-F., Troyer, M. & Soluyanov, A. A. Wanniertools: an open-source software package for novel topological materials. *Comput. Phys. Commun.* **224**, 405–416 (2018).